J. Fluid Mech. (2001), *vol.* 438, *pp.* 277–305. Printed in the United Kingdom

Noise sources in a low-Reynolds-number turbulent jet at Mach 0.9

By JONATHAN B. FREUND

Mechanical and Aerospace Engineering, University of California, Los Angeles, CA 90095, USA

(Received 15 July 1999 and in revised form 8 January 2001)

The mechanisms of sound generation in a Mach 0.9, Reynolds number 3600 turbulent jet are investigated by direct numerical simulation. Details of the numerical method are briefly outlined and results are validated against an experiment at the same flow conditions (Stromberg, McLaughlin & Troutt 1980). Lighthill's theory is used to define a nominal acoustic source in the jet, and a numerical solution of Lighthill's equation is compared to the simulation to verify the computational procedures. The acoustic source is Fourier transformed in the axial coordinate and time and then filtered in order to identify and separate components capable of radiating to the far field. This procedure indicates that the peak radiating component of the source is coincident with neither the peak of the full unfiltered source nor that of the turbulent kinetic energy. The phase velocities of significant components range from approximately 5% to 50% of the ambient sound speed which calls into question the commonly made assumption that the noise sources convect at a single velocity. Space–time correlations demonstrate that the sources are not acoustically compact in the streamwise direction and that the portion of the source that radiates at angles greater than 45° is stationary. Filtering non-radiating wavenumber components of the source at single frequencies reveals that a simple modulated wave forms for the source, as might be predicted by linear stability analysis. At small angles from the jet axis the noise from these modes is highly directional, better described by an exponential than a standard Doppler factor.

1. Introduction

Although a theoretical representation of the acoustic source in turbulent flow has existed for nearly 50 years (Lighthill 1952), precise measurements of any theoretical source in an actual turbulent jet has been impossible owing to experimental difficulties. The complexity of the acoustic source, typically defined statistically as a space–time correlation of fluctuating quantities, is the principal factor responsible for these difficulties. Confounding things further is the well-known fact that only the portion of the source with a supersonic phase velocity relative to the ambient flow will radiate noise to the acoustic far field. For jets whose dominant turbulent eddies convect subsonically, this means that only a very small portion of the acoustic sources actually radiate. This makes the noise difficult to predict and presents additional challenges to experimentalists attempting to educe acoustic sources, as it is insufficient to simply identify energetic structures in the jet. Essentially, it is the evolution of the energetic turbulent structures as they convect that is important, which makes the effective source time dependent in a way that compounds measurement difficulties.

Computing technology and numerical methods have recently reached a point where

turbulent jet noise can be computed from first principles and thus, provided that such simulations are properly validated, provide a characterization of the acoustic sources that has previously been lacking. The current study takes this approach. Although such simulations are limited to low Reynolds numbers, experimental data at Reynolds number 3600 are available (Stromberg, McLaughlin & Troutt 1980) and the jet computed at this Reynolds number is in excellent agreement with the data. The analysis of the noise sources in the simulated jet constitutes the principle contribution of this paper. Particular attention will be paid to isolating space–time Fourier modes that are capable of radiating to the acoustic far field.

In pursuing a definition for the noise sources in a jet, it often seems that a balance must be struck between rigour and ease of application. Consider, for example, Lighthill's (1952) well-known manipulation of the flow equations into a simple wave operator on density responsible for propagation and a group of terms he assumes to be analogous to an acoustic source,

$$\underbrace{\frac{\partial^2\rho}{\partial t^2} - a_\infty^2 \frac{\partial^2\rho}{\partial x_j \partial x_j}}_{\text{sound propagation}} = \underbrace{\frac{\partial^2 T_{ij}}{\partial x_i \partial x_j}}_{\text{'source'}}, \tag{1.1}$$

where ρ is the density, a_∞ is the ambient speed of sound and T_{ij} is the Lighthill stress tensor. This decomposition is known to be non-unique and is in some sense incorrect because flow–acoustic interactions are not distinguished from true acoustic sources. Nevertheless, considerable effort has gone into modelling the Lighthill source for jet noise prediction, and with some success (see the review by Lilley 1991). More intricate formulations, such as that of Lilley (1974) (see also Goldstein 1976), extend Lighthill's acoustic analogy approach by using a wave operator that accounts explicitly for some flow–acoustic interactions to provide what is perhaps a more complete representation of the mechanism. However this is done at the price of simplicity (Lilley 1991; Goldstein 1976), and is arguably not beneficial (Bailly, Lafon & Candel 1994) though a recent predictive approach does appear to benefit from making the distinction (Khavaran 1999). However, Lilley's equation also becomes ambiguous when it is linearized, as it must be for it to be interpreted. If this is done in such a way that the analogy remains exact, terms are shifted from the propagation operator into the source, which once again blurs their distinction.

A recent quantitative application of the linearized Lilley's equation to a two-dimensional mixing layer demonstrated some of the difficulties in using that equation to compute sources from simulation data (Colonius, Lele & Moin 1997). A conclusion from that study was that, depending upon how the analogy is formulated, the prediction is either sensitive to the parallel mean flow about which the equation is linearized, or the source is composed of very large nearly cancelling components that make numerical evaluation unreliable and interpretation difficult.

In this study flow–acoustic interaction is not considered explicitly and the term 'source' is meant in the sense of Lighthill's source. Dynamics that do not satisfy the classic homogeneous-medium second-order wave equation are grouped into this nominal source. For this reason we must be cautious in interpreting the results, as studies of multipole sources in parallel shear flow suggest that there are important flow–acoustic interactions in jets (Goldstein 1975, 1982). On the other hand, predicting the Lighthill source is equivalent to predicting the noise, and since there is currently no satisfactory quantitative model for jet noise, working with the Lighthill source may still turn out to be the best approach. We should also note that several

detailed theoretical criticisms of the analogy approach in general have appeared over the years (Doak 1972; Crow 1970; Fedorchenko 2000). However, since a more attractive alternative has not been offered, we will stick with Lighthill's theory in this study.

Increased insight into the mechanisms responsible for the creation of jet noise, especially at near-sonic jet velocities where noise is currently of concern for civilian aircraft, will aid predictive modelling efforts, and show the limits of different modelling approaches. The crudest of these use dimensional scalings derived from acoustic analogy expressions, the most famous of which is Lighthill's U^8 law for radiated intensity (Lighthill 1952). A more refined technique is to use acoustic analogies in conjunction with the Reynolds-averaged Navier–Stokes equations, with standard turbulence closures, for the mean flow. In this case, unsteadiness is modelled with empirical correlations derived from existing experimental data to predict the sound (Khavaran, Krejsa & Kim 1994; Khavaran 1999; Bailly *et al.* 1994, 1997). A drawback of this approach is that considerable approximations are required to express the noise sources in terms of turbulent kinetic energy k, for example, which would be predicted by the same k–ε turbulence model that solved the flow. Because of the empiricism involved, it is not clear how reliable such models will be away from the conditions for which they were designed. Solving unsteady equations with turbulence models to reduce the expense of solution promises to increase the flexibility of these models (Bastin, Lafon & Candel 1997), as do approaches built on parabolized stability equations (e.g. Yen & Messersmith 1999). A similar approach currently under development is large-eddy simulation for jet noise (Choi *et al.* 1999; Bogey, Bailly & Juvé 2000; Boersma & Lele 1999). Better understanding of the noise sources and in particular the capability to compute them directly will prove useful in validating the theoretical basis of these approaches as well as expose any of their inherent limitations.

Several researchers have assumed that the acoustic sources in subsonic jets are similar to instability waves that initially grow and then stabilize and decay as the jet's shear layers thicken. Crow (1972) and Ffowcs Williams & Kempton (1978) have built heuristic models for the sources of jet noise around this reasoning and Huerre & Crighton (1983) used a slowly spreading linear instability analysis to predict its form. These sources are not acoustically compact in the traditional sense, and so while they are nearly self-cancelling as quadrupoles, they are not strictly quadrupoles. Their exponential directivity, as observed experimentally in forced jets by Laufer & Yen (1983), precludes any multipole representation (Crighton & Huerre 1990). A contribution of this work is to show that the Lighthill source has a similar structure in an unforced jet, which is important for jet noise theories which assume that the sources are convecting quadrupoles (Lighthill 1954; Ffowcs Williams 1963). With regard to the commonly made assumptions of source compactness and multipole representation, Lighthill (1963) points out that these are low Mach number theories that are commonly extended beyond their range of strict applicability to near-sonic flows where there is more practical interest. The present results provide insight into how this extension begins to fail in a turbulent jet.

The paper is organized as follows. The flow parameters and necessary aspects of the numerical method are introduced in § 2 and the numerical results are validated in § 3 and § 4 which respectively address the turbulent jet flow and the radiated sound. In § 5, which constitutes the bulk of the paper, the Lighthill acoustic source is computed and analysed.

2. Preliminaries

2.1. *Flow parameters*

The subject of the present study is a Mach 0.9 round jet that exhausts into a quiescent infinite medium. This jet has a constant stagnation temperature ($T_j/T_\infty = 0.86$) and a Reynolds number $Re = \rho_j U_j D_j/\mu_j = 3600$. The subscript $(\ )_j$ denotes a nozzle exit condition, so ρ_j, U_j, D_j and μ_j are, respectively, the density, velocity, diameter and viscosity of the jet at the nozzle. These parameters and geometry match an experimental study conducted by Stromberg *et al.* (1980) and results will be compared to their data whenever possible.

Because this Reynolds number is well below that of jet engines, we should summarize the expected quantitative and even qualitative differences from high Reynolds number jet noise before proceeding. One is that we expect the noise to be more tonal than at higher Reynolds numbers because of the smaller range of energetic turbulence scales. This difference is particularly important because at jet engine scale these missing frequencies receive a significant weighting when adjusted for human annoyance. Also, the initial shear layers of the jet will also be laminar and therefore nearly silent relative to the turbulent flow downstream, which is certainly not the case at higher Reynolds numbers, so a potentially important portion of the source at high Reynolds number is missing. Nevertheless, since an accurate predictive capability for jet noise continues to elude modellers, it is hoped that some insights gleaned at this low Reynolds number might aid understanding and prediction of noise from jets at practical Reynolds numbers even though direct extrapolation of the present data may not be possible.

2.2. *Governing equations and numerical methods*

The compressible flow equations were formulated in cylindrical coordinates, as in Freund, Moin & Lele (1997), and solved numerically without modelling approximations. Radial and axial derivatives were computed with sixth-order-accurate compact finite differences (Lele 1992) and azimuthal derivatives were computed with Fourier spectral methods. A fourth-order Runge–Kutta scheme was used to advance the solution in time. The same basic algorithm was used by Freund *et al.* (1997) to study compressible turbulence in an annular mixing layer (see also Freund, Lele & Moin 2000) and the reader is referred there for its complete documentation. For the computation presented in this paper, the equations were discretized with $640 \times 250 \times 160$ mesh points in the axial, radial, and azimuthal directions respectively. The mesh was compressed radially with minimum spacing $\Delta r = 0.018 r_o$ at radial position $r = 0$ and axially with minimal spacing $\Delta x = 0.049 r_o$ at axial position $x \approx 20 r_o$, where r_o is the jet nozzle radius. The mesh spacing changed by less than 1% per mesh point. The azimuthal θ-mesh was, of course, uniform.

The region in which the flow equations were solved will be referred to as the physical portion of the computational domain. This extended $33 r_o$ in the streamwise direction and $8 r_o$ in the radial direction. Beyond this region in all directions, but on the same contiguous numerical mesh, dissipative terms were added to the equations in order to approximate anechoic boundary conditions. These boundary zones were not physical in the sense that no effort was made to imitate any physical mechanism in detail; their purpose was simply to approximate a radiation condition. In the downstream and radial directions the mesh was stretched and extended by $17 r_o$ and $12 r_o$ respectively beyond the physical domain. To damp disturbances in this zone, the solution was filtered using techniques similar to those of Colonius, Lele & Moin

	Δ per timestep	min	max
A	0.0001	0.01	0.07
St	0.00085	0.1	0.7
ϕ	0.00085	–	–
ψ	0.00085	–	–

TABLE 1. Parameters for inflow randomization.

(1993) so that all fluctuations were reduced to a negligible level by the time they reached the actual boundaries of the computational domain, where a characteristic boundary condition was applied. Details of this procedure are discussed by Freund (1999*b*).

Since it was deemed unnecessary to realistically simulate the nozzle in the present computations, an inflow boundary zone of width r_o was used to generate appropriate nozzle conditions with a technique similar to that used by Freund & Moin (2000). Writing the flow equations in the compact form $\boldsymbol{N}(\boldsymbol{q}) = 0$, where $\boldsymbol{q}$ is a vector of the flow variables, an additional term was added in the inflow boundary zone to drive the solution toward the desired nozzle exit conditions, $\boldsymbol{N}(\boldsymbol{q}) = -\sigma(\boldsymbol{q} - \boldsymbol{q}_{\text{target}})$, where σ was a large positive constant. The specified nozzle condition was a thin laminar annular shear layer with

$$\frac{\bar{v}_{x\,\text{target}}}{U_j} = \frac{1}{2}\left[1 - \tanh\left[b(\theta,t)\left(\frac{r}{r_o} - \frac{r_o}{r}\right)\right]\right]. \tag{2.1}$$

The factor b in (2.1), is a thickness parameter with a mean of 12.5, was varied in θ and t (time) to add small-amplitude random perturbations to seed the instabilities and turbulence. This excitation prevents auto-excitation of the jet by an unphysical feedback mechanism involving spurious numerical modes. Without this small excitation the disturbances did not saturate until further downstream after a significant distance of laminar spreading of the shear layers. Unfortunately, the disturbances at a laminar flowing nozzle exit are difficult to measure and are not available for the Stromberg *et al.* (1980) data, so the thickness factor $b(\theta,t)$ was modelled in an *at hoc* fashion as

$$b(\theta,t) = 12.5 + \sum_{m=0}^{2}\sum_{n=0}^{1} A_{nm}\cos\left(\frac{St_{nm}U_j}{D}t + \phi_{nm}\right)\cos\left(m\theta + \psi_{nm}\right), \tag{2.2}$$

where the nm subscripted terms were slowly varied in a random-walk fashion. At each simulation timestep, $\Delta t = 0.0085 r_o/a_\infty$, they were each increased or decreased by a small amount given in table 1. A pseudo-random-number generator determined the 1-in-20 chance at each timestep that the variation would change from increase to decreasing or vice versa. Limits on the variation are also given in table 1. In the 50 000 timesteps that were used to solve the flow (after a stationary state was achieved), all coefficients wandered significantly over their permitted ranges. The jet development was not found to be highly sensitive to the particular form of this low-amplitude random forcing at the nozzle, and white noise added at the nozzle produced similar results for the turbulence but also produced significant spurious noise. The present approach was chosen because such disturbances are approximately solenoidal and therefore quiet.

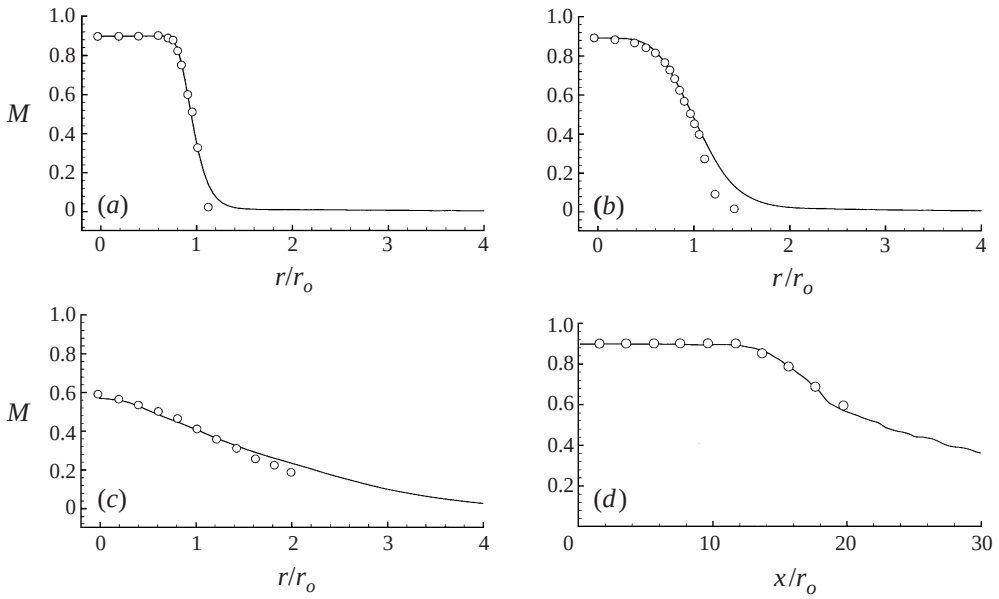

FIGURE 1. Mach number profiles from: ○, Stromberg *et al.* (1980); ———, present simulation. (*a*) $x/r_o = 2$; (*b*) $x/r_o = 10$; (*c*) $x/r_o = 20$; (*d*) jet axis ($r = 0$).

3. The turbulent jet flow

3.1. *Mean flow*

Mean Mach number profiles are shown in figure 1. Near the nozzle the profile has a typical top-hat shape (figure 1*a*) which then broadens as the flow develops downstream (figures 1*b*, *c*). Figure 1(*d*) shows the development of the Mach number on the jet axis. The mean potential core length is approximately $x = 14r_o$.

Also shown in figure 1 are data from the Stromberg *et al.* (1980) study. For comparison, the axial origin, $x = 0$, of the simulation has been placed 2 jet radii into the physical portion of the computation, or, equivalently, $3r_o$ from the edge of the computational domain (see §2.2). The offset of $2r_o$ was chosen to match the experiment at the first available measurement location, $x = 2r_o$. Given that the correct exit momentum thickness and disturbances levels are unknown, there is no reason to believe that the quality of the data would benefit from performing the numerous expensive iterations that would be necessary to remove this offset. Matching the data at the first reported measurement station is the best that can be done under these circumstances. In a sense, the region of the computation between the inflow computational boundary and the first experimental measurement location can be thought of as an artificial zone designed to match the experiment at $x = 2r_o$ and the data in this zone disregarded. However, since the flow equations were solved in this region, we treat it as realistic in this study. A similar justification can be made for not including a physically realistic nozzle in the simulation. All subsequent data will be presented with $x = 0$ corresponding to the nozzle location in Stromberg *et al.*'s experiment.

Given this minor adjustment, the agreement with the data is excellent. Differences are of only a few percent except near the outer edges of the jet where they increase significantly. It is believed that this disagreement is a consequence of using a Pitot probe to measure velocity where the mean flow was too small. In such circumstances,

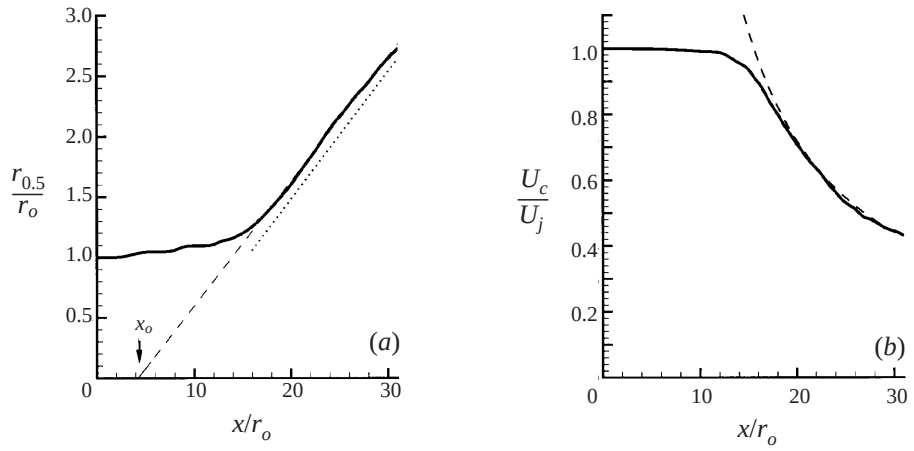

FIGURE 2. (*a*) The half-velocity radius: ———, of the jet with a visual linear fit and – – – –, to identify the virtual origin of the jet ($x_o = 4.15r_o$). A straight reference line (· · · · · ·) is also shown. (*b*) Centreline velocity: ———, the present simulation; – – – –, equation (3.1) with $B_u = 5.8$ (Hussein *et al.* 1994).

Pitot probe measurements are unreliable. Examination of the simulation database, assuming for now that it is at the very least qualitatively realistic, reveals that near the jet edge there is occasionally a locally reversed flow which would in itself render Pitot measurements inaccurate. Supporting this further, the experimentally measured points with $M \lesssim 0.3$ do not appear to always follow the same trends as the rest of the data (Stromberg *et al.* 1980).

At $Re = 3600$ the flow is expected to be laminar for a significant portion of the potential core region. However, after transition and downstream of the potential core we expect the mean flow to be independent of both viscosity and compressibility and eventually spread linearly with downstream distance as any turbulent free jet should. Experiments on high-Reynolds-number fully developed jets have shown that the centreline velocity, U_c, decays as

$$\frac{U_c}{U_j} = B_u \left[\frac{2r_o}{x - x_o} \right], \tag{3.1}$$

where x_o is the axial coordinate of the virtual origin of the jet and the constant B_u is approximately 5.8 (Hussein, Capp & George 1994). Figure 2(*a*) shows that linear growth of $r_{0.5}$, which is defined by $\bar{v}_x(r_{0.5}) = 0.5U_c$, begins almost immediately after the potential core closes in the present case. Likewise, figure 2(*b*) shows that (3.1) with $B_u = 5.8$ and $x_o = 4.15r_o$ matches the simulation data. This agreement is noteworthy because it suggests that compressibility is negligible here, at least with regard to mean flow development, and that our jet displays self-similar behaviour surprising early in its development. This will facilitate comparison to incompressible jet data in the following section. The agreement also verifies that it develops properly as a free jet despite the artificial boundary conditions imposed in the computation.

3.2. *Turbulence*

Two components of the Reynolds stresses are shown in figure 3. After an initial region of laminar flow, both components rise rapidly near the end of the potential core. For example, $\overline{v_x'v_x'}$ reaches only $0.010U_j^2$ by $x = 8r_o$. However, by $12.5r_o$, the fourth profile in figure 3(*a*), it has reached nearly its peak value of $0.041U_j^2$ suggesting that

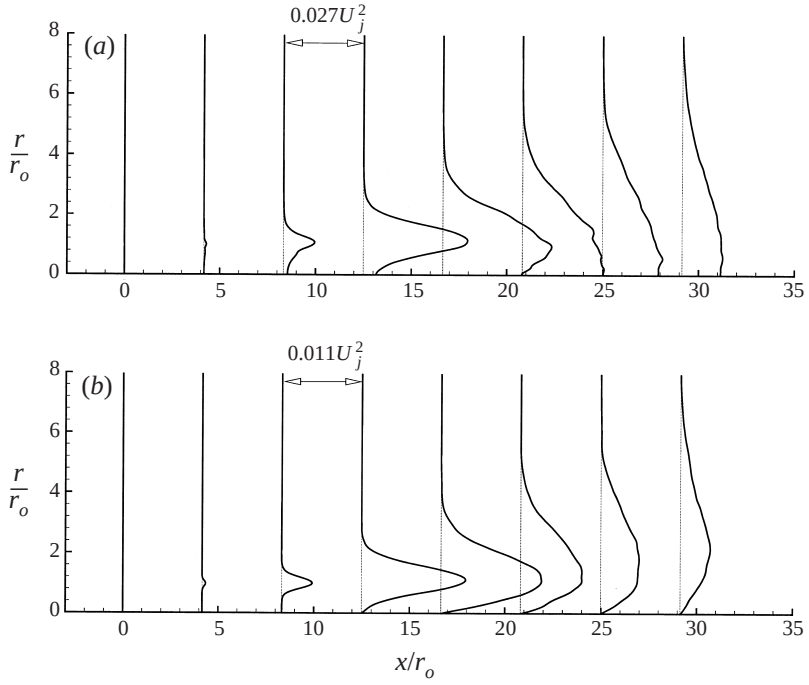

FIGURE 3. Reynolds stresses normalized by nozzle exit velocity: (*a*) $\overline{v_x'v_x'}$ and (*b*) $\overline{v_x'v_r'}$.

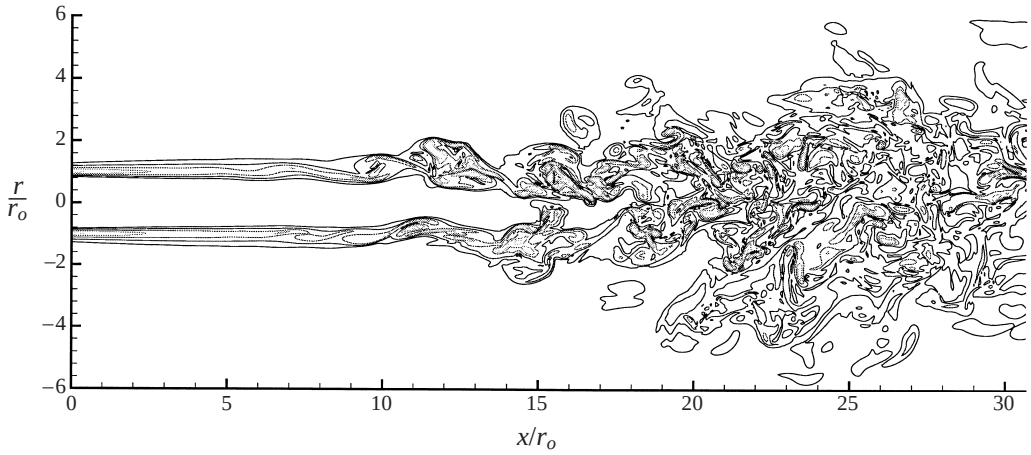

FIGURE 4. Instantaneous contours of vorticity magnitude: levels are $\omega r_o/U_j = 0.35, 1, 2, 3, 4$ with lighter contours representing larger values. Peak vorticity magnitude (not shown) was $\omega r_o/U_j = 11$.

a rapid nonlinear saturation and transition has occurred. The vorticity magnitude visualization provided in figure 4 supports this. The other Reynolds stresses follow a similar development.

No turbulent stresses were documented by Stromberg *et al.* (1980), but assuming that experimental limitations are indeed responsible for the discrepancies in the mean Mach number profiles at the edges of the sheared region, then it is reasonable to assume that the shear stress is accurate in the present simulation. This, however, offers no guarantee that a jet at this Reynolds number does indeed have the hallmarks of

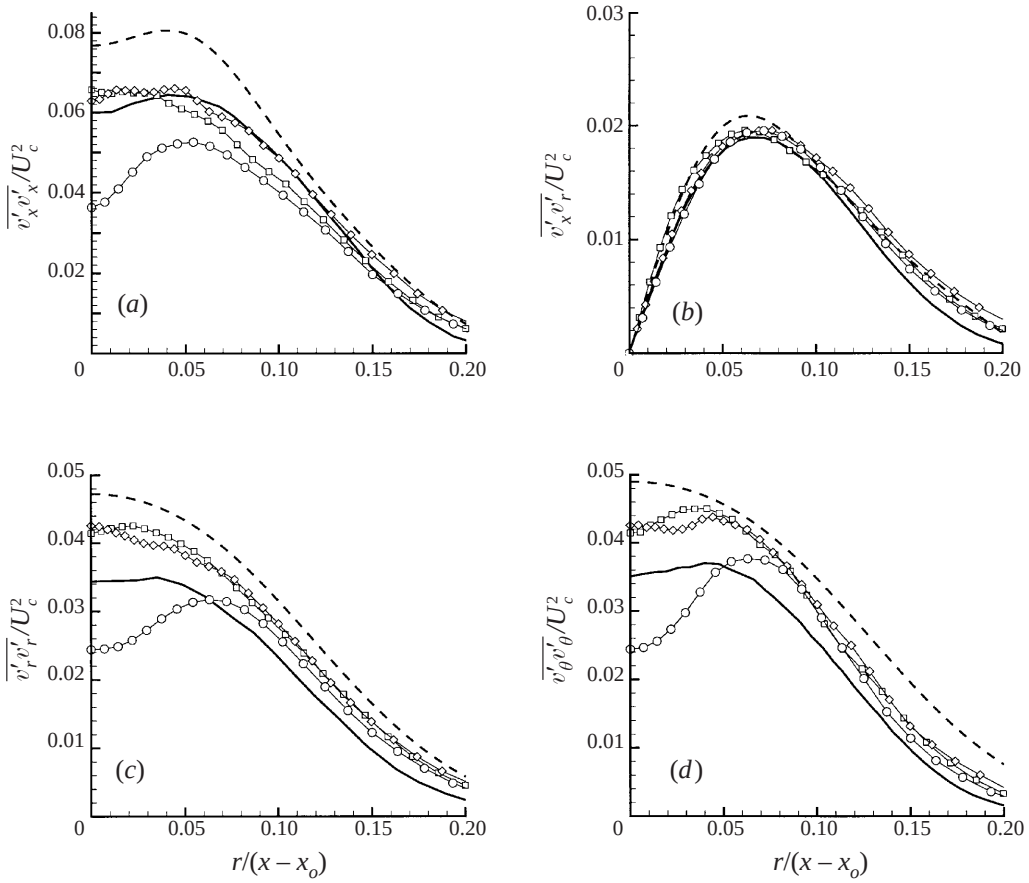

FIGURE 5. Second moments of velocity: ○, $x = 20r_o$; ◇, $x = 25r_o$; □, $x = 30r_o$; ———, low-Mach-number experimental data from Panchapakesan & Lumley (1993); and – – – –, low-Mach-number experimental data from Hussein *et al.* (1994). The Panchapakesan & Lumley (1993) profiles were digitized and replotted from the least-squares fits in their publication; the Hussein *et al.* (1994) profiles are the curve fits they provided. The simulation data were averaged in time for the entire simulation history and in space over a streamwise band of width $\Delta x_{\text{ave}} = 2r_o$.

turbulence: Reynolds stresses that are insensitive to Reynolds number, a broad-banded energy spectrum, rapidly decaying two-point correlations, and significant viscous dissipation of kinetic energy.

Concerning the Reynolds stresses, we now take advantage of the apparent self-similar behaviour discussed in the previous section and compare to incompressible jet data in figure 5. The agreement is good for all second moments of velocity when $x \gtrsim 25r_o$ and for the shear stress when $x \gtrsim 20r_o$. The simulation data almost without exception fall between the profiles measured by Panchapakesan & Lumley (1993) and Hussein *et al.* (1994). We conclude that the post-transition Reynolds stresses are realistically independent of viscosity.

Figure 6 shows one-dimensional axial and azimuthal turbulence energy spectra at the nozzle lip line ($r = r_o$). The axial spectrum (figure 6*a*) is indeed broad banded with the smallest scales having 10^6 times less energy than the largest. Azimuthal spectra in figure 6(*b*) show the downstream development of the jet turbulence. At $x = 0$ the spectrum is dominated by the low azimuthal mode numbers that are explicitly excited

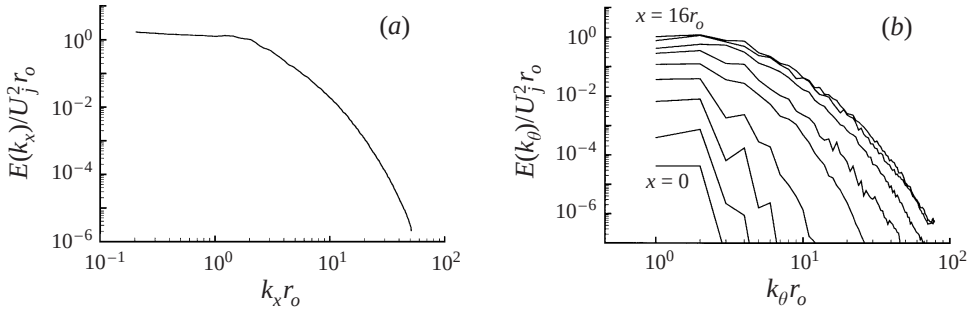

FIGURE 6. One-dimensional turbulence energy spectra at $r = r_o$: (*a*) x-direction, and (*b*) θ-direction at axial intervals of $2r_o$ starting at $x = 0$ (bottom curve) and ending at $x = 16r_o$ (top curve).

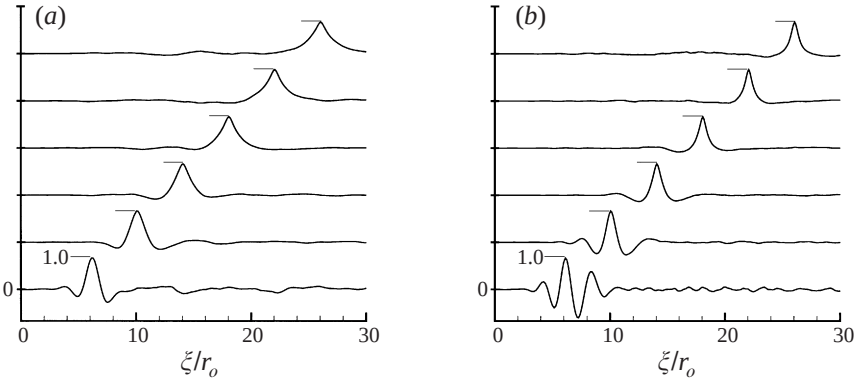

FIGURE 7. Two-point streamwise correlations at $r = r_o$ as defined in (3.2): (*a*) v_x'; (*b*) v_r'.

as discussed in § 2.2. Further downstream the spectra broaden and the peak energy component increases rapidly until $x = 14r_o$ which is near the end of the potential core and where the vorticity magnitude visualization in figure 4 suggests that the flow has transitioned. The spectrum does not change significantly downstream of $x \approx 16r_o$ (not shown). No inertial range is expected at this Reynolds number.

Axial two-point correlations defined as

$$\frac{\overline{v'(x)v'(\xi)}}{\overline{v'(x)v'(x)}} \tag{3.2}$$

are shown in figure 7 for $x = 6r_o$, $10r_o$, $14r_o$, $18r_o$, $22r_o$ and $26r_o$ and $v' = v_x'$ and v_r'. At $x = 6r_o$, where the visualization in figure 4 suggests that the flow is laminar with developing instability waves, the correlation is indeed wave-like, particularly for the radial velocity component. However, at larger x the correlations decay rapidly, indicative of turbulence. Neither integral length scale changes much past $x \approx 15r_o$.

Figure 8 shows the radially integrated turbulent kinetic energy production, mean flow transport, and viscous dissipation. (The compressible terms are included in the viscous dissipation, but they are very small at this Mach number.) All the budget terms not shown are less than 10% of the peak production (both individually and combined) and so are not discussed. The production, which begins to rise near $x = 6r_o$ in the laminar region, is initially balanced by mean transport. Only after $x \approx 13r_o$ does viscous dissipation act as the most significant removal mechanism. At $x \approx 18r_o$ the mean transport becomes positive, making the dissipation the only

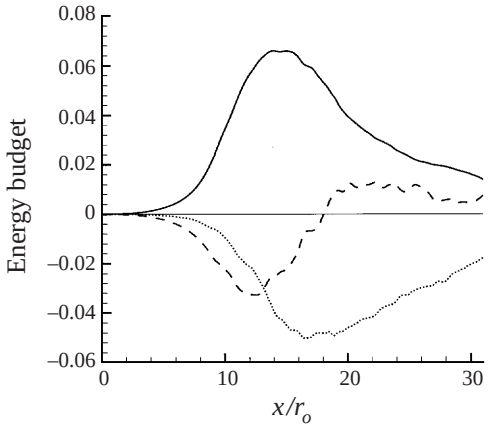

FIGURE 8. Radially integrated turbulence kinetic energy budget normalized by $\rho_j U_j^3/r_o$: ———, production; – – – –, mean flow transport; · · · · · ·, viscous dissipation.

significant sink. This balance corroborates the energy spectra in showing that the dissipation scales are well resolved.

4. The far-field sound

Of great concern in jets are the pressure fluctuations that decay most slowly away from the jet and thus constitute the far-field noise. Using a generally accepted guidance that several wavelengths are required to reach the point where this asymptotic decay rate becomes evident, it is clear that the $8r_o$ radial extent of the present simulation is too short and additional computation is required to reach the far field. Another motivation for extending the domain is that the noise data from Stromberg *et al.* (1980) are only available on an arc at $60r_o$, also well beyond the present Navier–Stokes computation.

Extending the solution to the far field is straightforward since at $r = 8r_o$ the flow is irrotational with mean Mach number less than 0.02 and disturbances are small ($p'/\bar{p} < 0.002$). Under these conditions, a linear wave equation accurately describes the pressure fluctuations. The details of the solution method used are described in the Appendix. The sound field dilatation is visualized in figure 9. The sound waves appear to emanate from roughly the end of the potential core and have an apparent peak intensity at 30° from the jet axis.

The sound pressure level on an arc at $60r_o$ from the nozzle is compared with experimental data in figure 10. Though a little high, the present results are well within the 3 dB uncertainty estimate provided with the Stromberg *et al.* (1980) data. When comparing with the higher Reynolds number data of Mollo-Christensen, Koplin & Martucelli (1964) and Lush (1971) in the same figure, it is clear that the lower Reynolds number jets are more directive. It should be noted that the Lush data are adjusted from $240r_o$ down to $60r_o$ and still show reasonable agreement, which suggests that the other measurements do not have significant near-field influences. A preliminary report on the present simulations showed essentially the same directivity though with a smaller statistical sample (Freund 1999*a*) using a different scheme to compute the far-field noise (Freund 2000).

Figure 11 compares the noise frequency spectrum at 30° from the jet axis with the Stromberg *et al.* data. Only a relative scale was given with those data so it has been

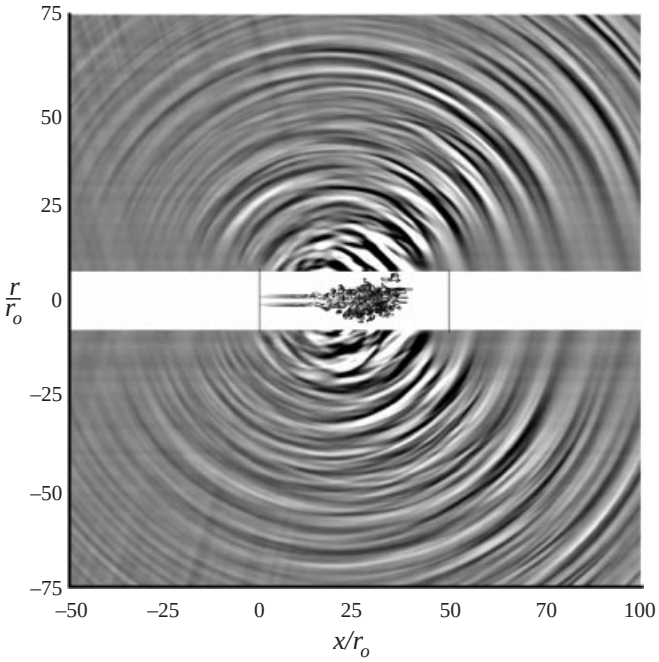

FIGURE 9. Visualization of the far-field sound: Black is $\Theta = \nabla \cdot \boldsymbol{u} < -0.0005 a_o/r_o$ and white is $\Theta > 0.0005 a_o/r_o$. The grey scale varies continuously between these extrema. The jet is visualized with contours of vorticity magnitude as in figure 4. The axial boundaries of the numerical domain (including the boundary zone) are demarked by the vertical lines. Only radiating modes are shown (see Appendix). Note that because of the geometry of the computational domain there is a blockage effect that decreases the sound near the axis in both the upstream and downstream directions. Some degree of blockage is unavoidable when computing the sound upstream and downstream of the flow computation. Geometrical reasoning suggests that sound radiating at less than $\alpha \approx 20^\circ$ may not be accurate.

adjusted vertically in the figure. Agreement is encouraging. In both cases the peak is near $St_D = 0.2$ and both spectra follow a similar decay with increasing frequencies. The peak for the present computation is somewhat sharper, but some disagreement is not surprising since nozzle conditions of the experiment were unknown. Overall, the *ad hoc* nozzle treatment used in this computation does a reasonable job at reproducing the experimental observations. Despite the accelerated decay of both spectra at high frequencies due to the low Reynolds number, the spectrum is continuous. It drops from its peak of 115 dB at $St_D \approx 0.2$ to around 60 dB at $St_D = 3.0$.

5. Acoustic sources

This section addresses the sources of noise in the jet. For present purposes these are defined as in (1.1) despite the ambiguities in Lighthill's (1952) approach concerning flow–acoustic interactions discussed in § 1. In defining the present source, the pressure is used as the acoustic variable as opposed to the density in Lighthill's original formulation, but otherwise the equations and reasoning are Lighthill's. By exact manipulations, the flow equations become

$$\frac{\partial^2 p}{\partial t^2} - a_\infty^2 \Delta p = S, \tag{5.1}$$

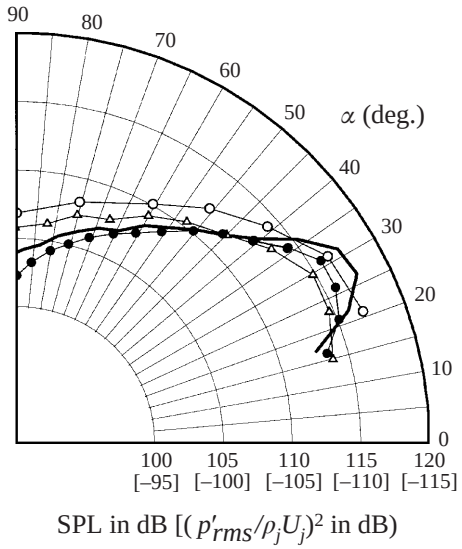

FIGURE 10. Overall sound pressure level (and acoustic intensity in brackets) directivity on an arc at $60r_o$ from the nozzle and with α measured from the jet axis: ———, $Re = 3600$ present study; ●, $Re = 3600$ Stromberg *et al.* (1980) experimental data; ○, $Re = 2 \times 10^5$ Mollo-Christensen *et al.* (1964) experimental data; △, $Re = 6 \times 10^5$ Lush (1971) experimental data (adjusted by 12 dB from 240 jet radii to 60).

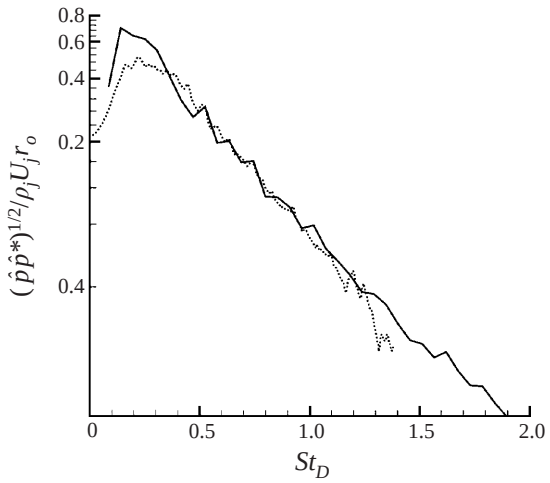

FIGURE 11. Far-field pressure spectrum at $\alpha = 30$: ———, present simulation; ·····, measurement of Stromberg *et al.*

where

$$S = a_\infty^2 \left[\frac{\partial^2 \rho u_i u_j}{\partial x_i \partial x_j} - \frac{\partial^2 \tau_{ij}}{\partial x_i \partial x_j} \right] + \frac{\partial^2}{\partial t^2}(p - a_\infty^2 \rho) \tag{5.2}$$

is the nominal acoustic source. The choice of pressure as the acoustic variable is motivated by the fact that pressure, having a nearly uniform mean in a free shear flow, is at times more convenient to use than the density. None of the results depend upon this choice.

Fourier integral methods were used to compute S and thereby provide its spectral makeup. The Fourier integral transform of the pressure in the streamwise direction and time and the simultaneous discrete Fourier transform in the azimuthal direction was defined by

$$\hat{p}_n(k,r,\omega) = \sum_{j=0}^{N_\theta-1} \int_{-\infty}^{\infty}\int_{-\infty}^{\infty} p(x,r,\theta_j,t)w(t)\,\mathrm{e}^{\mathrm{i}\omega t}\mathrm{e}^{\mathrm{i}kx}\mathrm{e}^{\mathrm{i}n\theta_j}\,\mathrm{d}t\,\mathrm{d}x, \tag{5.3}$$

with inverse

$$p(x,r,\theta_j,t) = \frac{1}{4\pi^2 N_\theta}\sum_{n=-N_\theta/2}^{N_\theta/2-1}\int_{-\omega_m}^{\omega_m}\int_{-k_m}^{k_m}\hat{p}_n(k,r,\omega)\,\mathrm{e}^{-\mathrm{i}\omega t}\mathrm{e}^{-\mathrm{i}kx}\mathrm{e}^{-\mathrm{i}n\theta_j}\,\mathrm{d}\omega\,\mathrm{d}k. \tag{5.4}$$

In practice, only a finite number of wavenumbers k and frequencies ω were computed, with integration bounds k_m and ω_m in (5.4) set by the resolution in x and t. The infinite bounds on the integral over x in (5.3) are of course unphysical, but in the same sense that the mathematical model of a jet exhausting into an infinite quiescent medium is an idealization. Downstream in experiments there are typically diffusers and settling chambers; similarly, in the present simulation there is the zonal boundary that damps the turbulence and noise. Because pressure fluctuations become negligible in this boundary zone, the infinite upper bound in (5.3) will give the same result as a finite upper bound that includes the data in the outflow boundary zone (this is shown subsequently). Similarly, the upstream flow is laminar without significant pressure fluctuations and so the same is true for the lower x-integration bound. Thus the infinite x-integral in (5.3) is equivalent to a finite integral from the laminar inflow through the boundary zone.

The infinite time-domain transform is also not well defined physically and in reality the jet must be started and eventually stopped. While the low frequencies associated with this are easily neglected in an experiment because the jet can be run for a relatively very long time, a limited time history is available from the simulation so care must be taken to avoid the introduction of spurious effects. To confine spurious spectral contributions to very low wavenumbers, $w(t)$ was included as a factor in the forward transform (5.3) with the functional form

$$w(t) = \frac{1}{2}\left[\tanh\left(5\frac{t-t_1}{t_1-t_0}\right) - \tanh\left(5\frac{t_f-t}{t_f-t_2}\right)\right]. \tag{5.5}$$

Times t_0 and t_f in (5.5) are respectively the time in the simulation when it was determined to be statistically stationary and the final time and t_1 and t_2 are respectively the 5% and 95% points in this time series. An example time series of pressure perturbations p' multiplied by $w(t)$ is shown in figure 12. It is clear that the $w(t)$ factor does not significantly affect the pressure for a large region in the middle of the time series. Since the maximum distance between two points in the computational domain is approximately $38r_o$, by computational time of approximately $t_0+2(t_1-t_0)+38r_o/a_\infty$ we expect the sound to be unaffected by the procedure outlined here.

Multiplying p by $w(t)$ is similar to a windowing operation common in signal analysis. However, by evaluating the integrals with a quadrature scheme with sufficiently fine discretization (trapezoidal rule was used) rather than applying a discrete transform the artificial periodic extension of the data beyond the available times series is effectively eliminated. The Fourier representation of the pressure computed by (5.3) is exact in the sense that subsequent evaluation of (5.4) reproduces the original 'windowed'

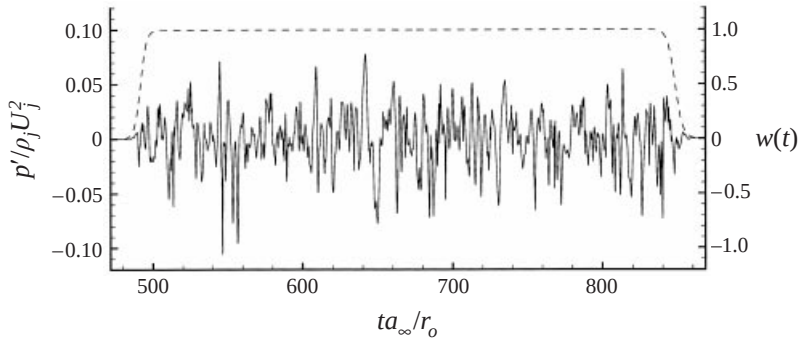

FIGURE 12. 'Windowed' pressure history at $(x, r, \theta) = (18r_o, r_o, 0)$. Also shown (right axis) is $w(t)$ from (5.5).

pressure time profile. However, artificial low frequencies are necessarily added to the spectrum due to the truncation. Since the transform of $w(t)$ decays reasonably slowly, these are confined to low frequencies.

5.1. *Lighthill's equation*

To verify that the techniques outlined above are capable of producing a reliable representation of the pressure in wavenumber–frequency space, the Lighthill source is computed in the transformed space and then used to compute the sound field. The agreement of this prediction with that from the direct numerical simulation will validate the transform methods and other aspects of the solution. Barring any numerical or systematics errors, the agreement should be perfect. However, given the expected susceptibility of aerodynamic noise computation to errors (Crighton 1993) such a validation is important. The sound after all is over 10^3 time less energetic than the flow and therefore particularly sensitive to errors.

From (5.1) and (5.3), the source in transformed space is simply

$$\hat{S}_n = \frac{\partial^2 \hat{p}_n}{\partial r^2} + \frac{1}{r}\frac{\partial \hat{p}_n}{\partial r} + \left[\omega^2 - k^2 - \frac{n^2}{r^2}\right]\hat{p}_n, \tag{5.6}$$

with inverse transform S defined analogously to p in (5.4). Figure 13 shows that S is small near the 'nozzle' where the flow is laminar. Levels are highest near the end of the potential core which is approximately where the turbulence is most intense (see figure 3). The source again becomes small by $x \approx 30r_o$.

Given S computed via (5.6), equation (5.1) was solved directly using the same numerical method as the flow solver. The Lighthill and directly computed Navier–Stokes solutions are compared on a ray in figure 14. Agreement is not perfect, but it is indeed very good. Likely causes of the small disparity are the inexact time transform discussed above or boundary conditions. Care was taken for both the Lighthill and Navier–Stokes solutions to ensure that all boundary conditions were approximately anechoic, but as in experiments this is not exact. Nevertheless, the agreement is good enough to demonstrate that the source is well represented in (k, ω)-coordinates. An instantaneous rather than statistical comparison was made because instantaneous agreement is the stronger condition and statistical agreement should follow. The curves shown in figure 14 are typical of all directions and times.

Bastin *et al.* (1997) claim that using the streamwise wavenumber as in (5.6) is 'not suitable' for computation of the Lighthill source, but if this cannot be done it is unclear how reliable the ω, k representation of the source would be. It is likely that

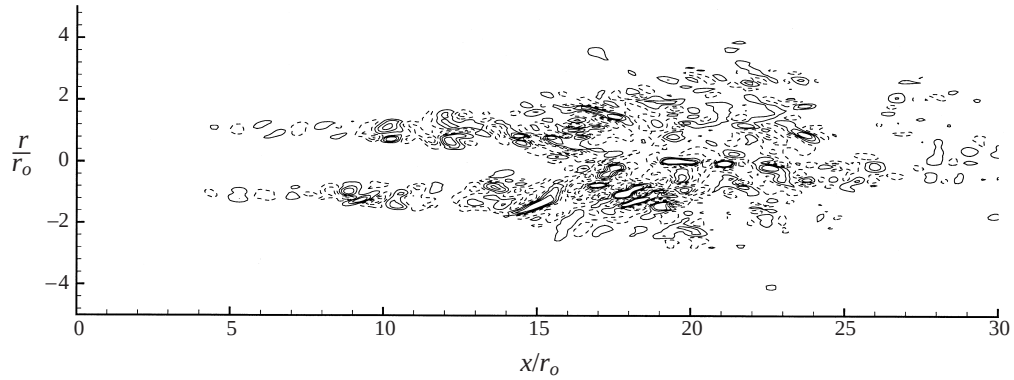

FIGURE 13. Instantaneous visualization of S, the Lighthill source. Contours: 6 evenly spaced levels between $S = \pm 2.5\rho_j U_j^2/r_o^2$. Positive levels are solid, negative levels are dashed. At this instant, $S_{\min} = -4.3\rho_j U_j^2/r_o^2$ and $S_{\max} = 8.45\rho_j U_j^2/r_o^2$.

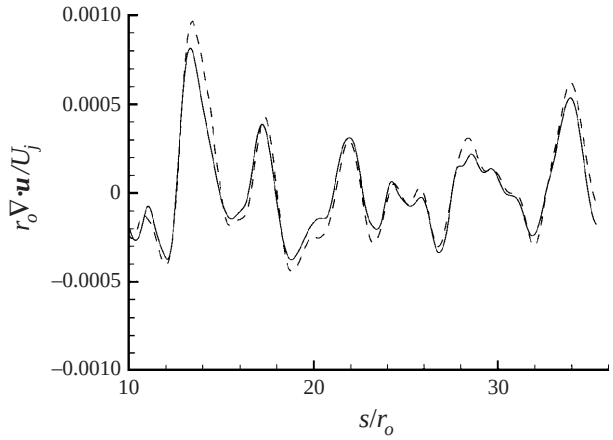

FIGURE 14. Comparison of dilatation on a ray from $x = 18r_o$ and inclined at 45° from the jet axis: ———, direct numerical simulation; – – – –, Lighthill's equation.

the two-dimensional transformed source they analysed is equally reliable despite their concerns.

5.2. *Source location*

Contour plots of the root-mean-squared (r.m.s.) full source and the radiating portion (to all angles) of the source defined by†

$$\hat{S}_{r_n}(k,\omega,r) = \begin{cases} \hat{S}_n(k,\omega,r) & \text{if} \quad \omega > ka_\infty, \\ 0 & \text{otherwise,} \end{cases} \tag{5.7}$$

are shown in figures 15(*a*) and 15(*b*) respectively. Although the statistical convergence for the full source is imperfect, it is nevertheless immediately obvious that the radiating portion of the source (figure 15*b*) has a different character to the full source

† This filtering operation leaves a set of modes capable of radiating to the far field in r, but it is not guaranteed to remove all non-radiating components of the Lighthill source. Additional cancellation may occur due to the radial structure of the source which is not accounted for in this analysis.

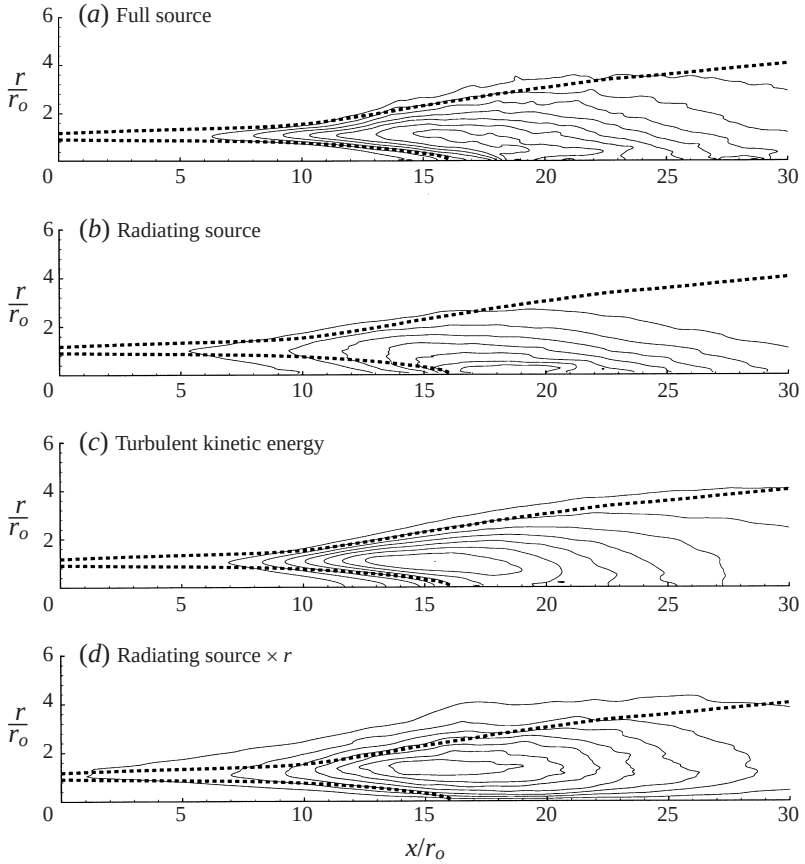

FIGURE 15. Contours of (*a*) r.m.s. S with 9 evenly spaced contours between 0 and $3.2\rho_j U_j/r_o^2$; (*b*) r.m.s. S_r with 9 evenly spaced contours between 0 and $2.1\rho_j U_j/r_o^2$; (*c*) turbulent kinetic energy $\overline{\rho(v_x'v_x' + v_r'v_r' + v_\theta'v_\theta')}$ with 9 evenly space contours between 0 and $0.056\rho_j U_j^2$; and (*d*) $S_r \times r$ with 9 evenly spaced contours 0 and $1.15\rho_j U_j^2/r_o^3$. The thick dotted lines show the $\bar{v}_x = 0.1U_j$ and $\bar{v}_x = 0.9U_j$ isolevels to indicate the extent of the jet.

(figure 15*a*). The filtered source (5.7) peaks on the jet axis just downstream of the end of the potential core, whereas the full source peak extends farther away from the jet axis into the shear layers. The full source also decreases more rapidly upstream than does the filtered source.

The turbulent fluctuations are, of course, responsible for the noise and so the intensity of the turbulence must be related to the source intensity. However, this relationship is not necessarily simple as is evident in figure 15(*c*) where the turbulence kinetic energy is seen also to have a distinctly different character to the radiating portion of the Lighthill source (figure 15*b*). The turbulent kinetic energy is evidently more similar to the full source than the radiating source defined by (5.7). It is plainly peaked within the shear layer, well upstream of the radiating source peak. Given this result, one must be extremely careful when making estimates of the source location or intensity based on the turbulent kinetic energy or similar quantities.

Though useful in showing the intensity of the radiating source, the data presented in figure 15(*b*) do not explicitly show where the bulk of the noise appears to come from because the volume of the acoustic sources is not taken into account. For

example, the contribution from very near $r = 0$ is negligible. To present a clearer picture of the volume-weighted contribution to the noise, r.m.s. S_r is multiplied by r and replotted in figure 15(d). Because the region around $r \approx r_o$ has potentially the greatest contribution to the far-field sound by this crude measure, this region will be studied in the greatest detail for the remainder of the paper.

The distribution of the sources computed here is not expected to be universal because the location of the sources is likely to depend to some degree upon the Reynolds number. As far as the present flow is concerned, decreased viscosity would tend to make the initial shear layers turbulent which would increase the acoustic radiation from that portion of the flow. However, the observation that the peak of the radiating portion of the source may occupy a different region in space than the peak of the turbulent kinetic energy has important consequences when modelling jet noise in general.

5.3. *Convection of the acoustic sources*

The convection of the acoustic sources is very important, a fact that has been well understood since the pioneering work of Lighthill (1952). Its importance lies in its being the primary cause for the source to fluctuate in time when observed from a stationary frame of reference, but the fluctuations leading to noise radiation constitute only a portion of these. Crighton (1975) provides a particularly lucid summary of earlier efforts analysing the role of source convection (Lighthill 1952, 1963; Ffowcs Williams 1963; Mani 1974). He shows that apparent fluctuations in time caused solely by the subsonic convection of unchanging sources do not radiate noise. Instead it is the change of the eddie sources as they convect that is responsible for the radiated sound.

To understand how S structures convect, it is instructive to first visualize S in an (x,t)-plane as is done in figure 16 for $r = r_o$ and $\theta = 0$. There are several notable features in this plot. First, it is immediatly evident that at this radial location there exists a prefered convection velocity which is approximately $0.6U_j$ as is commonly observed for turbulence in jet shear layers (this is treated more quantitatively below). It is also evident that the sources are both stronger and more organized before the potential core closes at around $x = 14r_o$. This is in accord with the fact that large organized coherent structures are more commonly observed in the shear layer portion of jets than in the transition or fully developed downstream regions, but may be in part an artifact of the low Reynolds number. Interestingly, downstream of the potential core the sources visualized in the figure (for the threshold values used) are still oriented at roughly the same angle despite the fact that the mean flow has decreased (see figure 1 and figure 23). Sources with $|S| > 0.5\rho_j U_j^2/r_o^2$ are, however, more intermittent and less regular in this region. In the neighbourhood of the end of the potential core, the sources are both strong and rapidly changing (the patterns in the (x,t)-plane are far less regular here than in the shear layers). According to the reasoning of Crighton (1975) and others discussed above, this is therefore where most of the far-field sound should arise, which appears to be the case in figure 9.

These notions are better quantified in terms of the phase-velocity makeup of the source. Figure 17 shows

$$S(k,\omega) = \frac{1}{N_\theta}\sum_{n=0}^{N_\theta}\int_0^{8r_o} |\hat{S}_n(k,\omega,r)|r\,\mathrm{d}r \tag{5.8}$$

which is a volume-averaged source for the whole of the computed jet. Because the

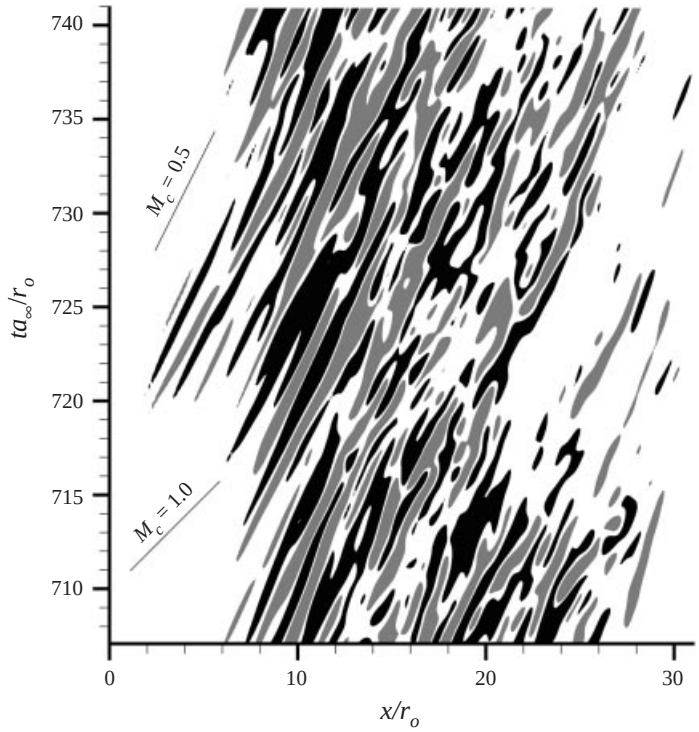

FIGURE 16. Space–time diagram showing the convection of the acoustic source S at $r = r_o$, $\theta = 0$. White: $|S| < 0.5\rho_j U_j^2/r_o^2$; grey: $S > 0.5\rho_j U_j^2/r_o^2$; and black: $S < -0.5\rho_j U_j^2/r_o^2$. The line segments indicated the slopes that would be expected for two convection Mach numbers.

statistical sample size available from the simulation data is small it was necessary to smooth the data significantly to construct intelligible contour lines in the (k, ω)-plane. Also, it was found that the 'windowing' procedure discussed in the introduction to this section contaminated $\hat{S}_n$ in regions of the (k, ω)-plane where $|\omega| < 0.05|k|a_\infty$ (regions that do not radiate noise). For presentation purposes, the contours here were reconstructed by extrapolating from the uncontaminated regions. For these reasons the details in figure 17 should only be interpreted qualitatively, though the general shape of the contours is reliable.

Not surprisingly, the strongest sources fall into a region where $|\omega/a_\infty k| \lesssim 0.6U_j/a_\infty$ ($M_c < 0.5$, where M_c is the convection speed divided by the ambient speed of sound) verifying that the convection speed of sources does not much exceed half the jet velocity. In this sense, figure 17 is similar to a prediction make by Ffowcs Williams (1963). However, here the mean phase velocity of the source appears to be approximately $0.36U_j$, or $M_c = 0.3$, which is lower than the $0.6U_j$ speculated by Ffowcs Williams. A potential factor contributing to this difference is that regions downstream of the shear layer, where the convection velocity of structures is expected to be a good deal smaller than $U_c \approx 0.6U_j$ as typically observed in the shear layer regions, are included in S. This is accentuated by the fact that the present shear layers are for the most part laminar and therefore will not make significant contributions to S. Nevertheless, a wide range of convection velocities are observed which has implications for directivity models that use Doppler factors $(1 - M_c \cos\alpha)^{-n}$ with a single convection velocity (Ffowcs Williams 1963; Lighthill 1952; Goldstein 1991).

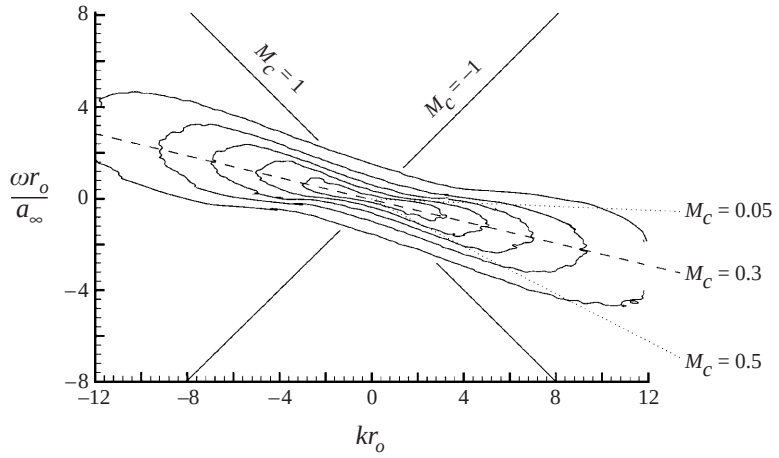

FIGURE 17. The acoustic sources in frequency–wavenumber space. The contours level indicates the relative contribution of (5.8) for particular k, ω pairs, but this result is meant to be interpreted qualitatively (see text).

Figure 17 is also similar to a plot made of sources in a two-dimensional unsteady Reynolds-averaged simulation by Bastin *et al.* (1997), but the sources in that study are more confined to the $|\omega/a_\infty k| \approx 0.6U_j$ line, which is probably a consequence of only computing the largest two-dimensional structures.

The bulk of this integrated acoustic source does not satisfy the condition that $|\omega/k| > a_\infty$ which is necessary for acoustic radiation to the far field in r. Nearly all of it will only spawn evanescent pressure waves which become negligible within a few wavelengths from the jet.

Figure 18 shows quantitatively the axial spectrum of four individual frequencies. Here the spectra were averaged in narrow bands ($\omega = \pm 0.02$) around the given frequency. The symmetry apparent in figure 17 was also used to converge the spectral statistics and the contributions from all azimuthal modes are included. At $\omega = 0.5a_\infty/r_o$, the spectral peak is close to the region capable of radiating to the far field (demarked in the figure by the straight vertical lines). As the frequencies considered increase (figure 18*b–d*), the spectral peaks move to higher (more negative) wavenumbers and levels fall more before the radiating $|ka_\infty| < |\omega|$ region.

5.4. *Filtering non-radiating source components*

The objective of this section is to better characterize the portion of the acoustic sources that radiates to the far field in r. This is undertaken by filtering non-radiating components of S by

$$\hat{S}_{f_n}(k, \omega, r; k_c) = \begin{cases} \hat{S}_n(k, \omega, r) & \text{if} \quad k < k_c, \\ 0 & \text{otherwise,} \end{cases} \tag{5.9}$$

where k_c is a cut-off wavenumber. For $k_c > \omega/a_\infty$, there should be no effect of this filtering procedure on the far-field sound.

Results are clearest if $\hat{S}_{f_n}$ is analysed in physical coordinates at a single discrete frequency and azimuthal mode number. This is done by inverse transforming to find the real space (function of x) component of a single frequency, designated ω_o, and

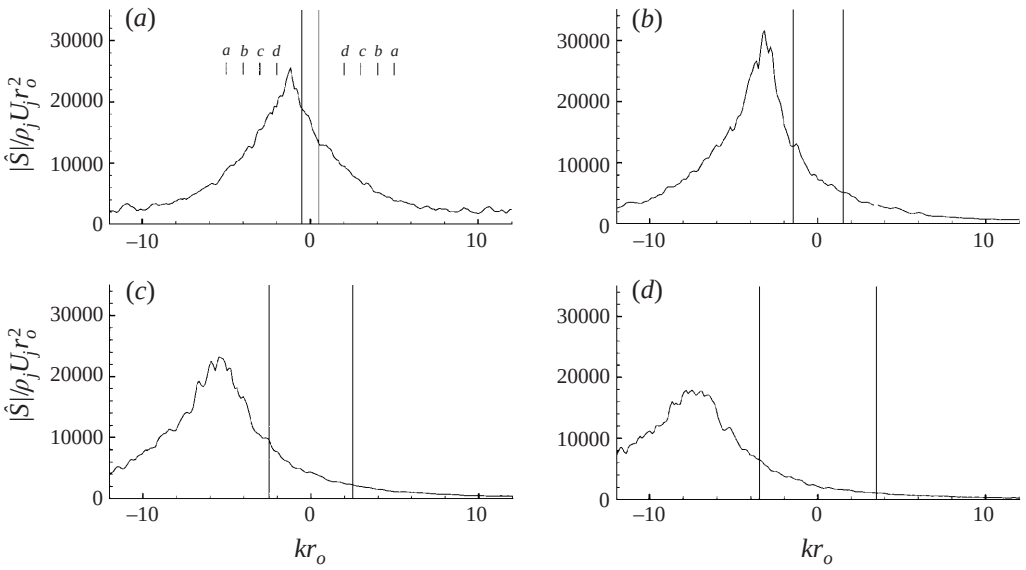

FIGURE 18. Axial wavenumber spectra at $r = r_o$ at individual frequencies: (*a*) $\omega = 0.5a_\infty/r_o$; (*b*) $\omega = 1.5a_\infty/r_o$; (*c*) $\omega = 2.5a_\infty/r_o$; (*d*) $\omega = 3.5a_\infty/r_o$. The labelled marks in (*a*) correspond to filter widths used in constructing figure 19(*a–d*). The vertical lines demark the region where $|k|a_\infty < \omega$.

azimuthal wavenumber, designated n_o:

$$S_f(x, r, \theta, t) = \frac{\mathrm{e}^{-\mathrm{i}\omega_o t}\mathrm{e}^{-\mathrm{i}n_o\theta}}{4\pi^2 N_\theta} \int_{-\infty}^{\infty} \hat{S}_{f_{n_o}}(k, \omega_o, r)\, \mathrm{e}^{-\mathrm{i}kx}\, \mathrm{d}k. \tag{5.10}$$

Thus S_f depends on all space coordinates and time, but the θ and t dependence is trivial. The peak frequency of the radiation is at approximately $\omega_o = 0.5a_\infty/r_o$, which corresponds to a Strouhal number of $St_D \approx 0.2$, and so makes this frequency particularly important. All significant frequencies in the far-field sound show similar results when the corresponding sources are analysed. Azimuthal mode $n_o = 0$ was picked for this illustration but the results are similar for all small n. Taking $k_c = 5/r_o$ in (5.9), transforming this single frequency of the source to physical coordinates, arbitrarily choosing $t = 0$ and $\theta = 0$ in (5.10), and picking $r = r_o$ leads to the curve shown in figure 19(*a*). As expected from the visualized source in figure 13, S_f rises from zero in the laminar region near $x = 0$ to a peak near the end of the potential core and then falls again toward zero by the right-hand side of the physical domain (at $x = 30r_o$). The curve is extended into the buffer zone of the computation where artificial filtering forces all fluctuations to zero. The implications of doing this were discussed in the introduction to this section on sources.

No clear structure is evident in figure 19(*a*), which is not surprising as it is an instantaneous trace in a turbulent flow, but it also shows a significantly broader range of streamwise wavenumbers than are capable of radiating noise to the far field at this frequency. These are filtered away in steps in figure 19(*b–d*) by decreasing k_c in (5.9). Additional filtering will result in a loss of the approximately compact support the profiles have in figure 19(*a–d*) and the connection to the physical structures in the jet would therefore be lost if the filtering procedure were carried further. It is clear that retaining only $k < 2/r_o$ gives a very simple form for the source (figure 19*d*), and it is worth reminding the reader at this point that all source components capable of radiating to the far field have been retained. The form in figure 19(*d*)

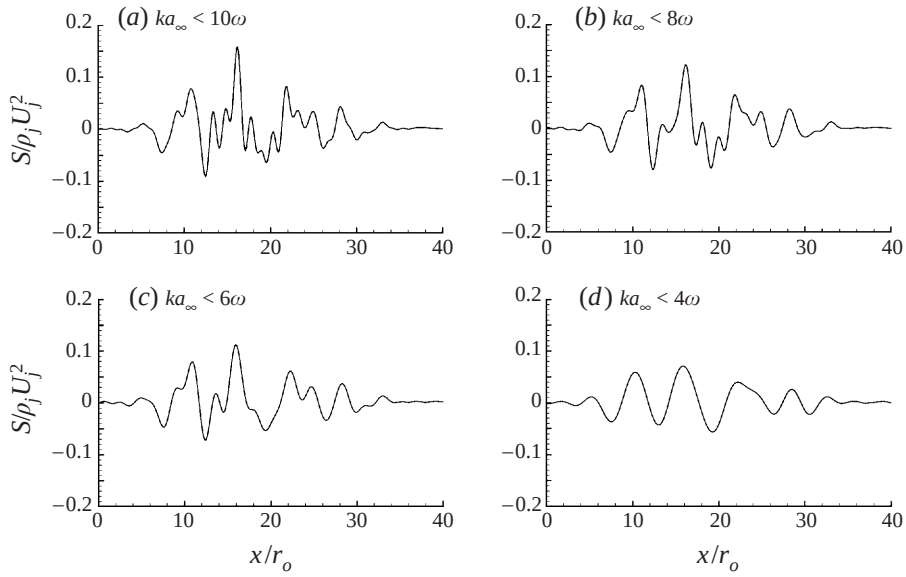

FIGURE 19. (*a–d*) The result on the streamwise source profile of a succession of streamwise wavenumber filters applied to the $\omega = 0.5 r_o/a_\infty$ component of the source at $r = r_o$. The corresponding source is shown in wavenumber coordinates in figure 18(*a*). The filter widths are also shown on that figure.

was also observed by Colonius *et al.* (1997) in a detailed study of a two-dimensional compressible mixing layer. Though it was not possible to measure the Lighthill source experimentally, Laufer & Yen (1983) found evidence of such organization in the early development of a weakly forced jet shear layer. Here for the first time it has been explicitly shown that upon filtering of the source data the Lighthill source has this form even past the end of the potential core in a turbulent jet.

Because the curve in figure 19(*d*) has the appearance of a growing and decaying instability wave, one might question whether or not it is an artifact of the low Reynolds number of the turbulence and merely an extension of the instability wave in the initially laminar shear layers. The evidence supporting realistic turbulence presented in § 3.2, in particular the rapidly decaying two-point correlations, suggests that this is not the case. In addition, a similar modulated wave form was educed by Arndt, Long & Glauser (1997) using a proper orthogonal decomposition of the near-field pressure fluctuations of a Reynolds number 4×10^4 jet. Though near-field pressure fluctuations are different to the Lighthill source, their results suggest that the observed form may persist at much higher Reynolds numbers than can be simulated.

5.5. *Sound from individual modes*

Crighton & Huerre (1990) studied model noise sources of the form seen in figure 19(*d*) and showed their noise intensity, I, to be what has come to be called superdirective,

$$I \sim \exp\left[A \cos\alpha\right], \tag{5.11}$$

where A is a constant. This form is in general agreement with the forced jet experiments of Laufer & Yen (1983). The noise from the single frequency and single θ-mode of the source plotted in figure 19(*d*) is visualized in figure 20. It is clearly very directional, but decays at small angles from the jet axis counter to (5.11) possibly because of refraction or the geometrical limitation of the finite Navier–Stokes computational domain. The

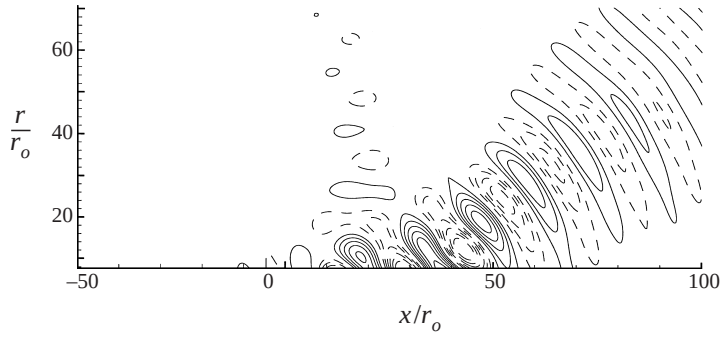

FIGURE 20. Noise from the source in figure 19(*d*). Contours of divergence of velocity: $-3 \times 10^{-5} U_j/r_o$ to $+3 \times 10^{-5} U_j/r_o$ with spacing $5 \times 10^{-6} U_j/r_o$.

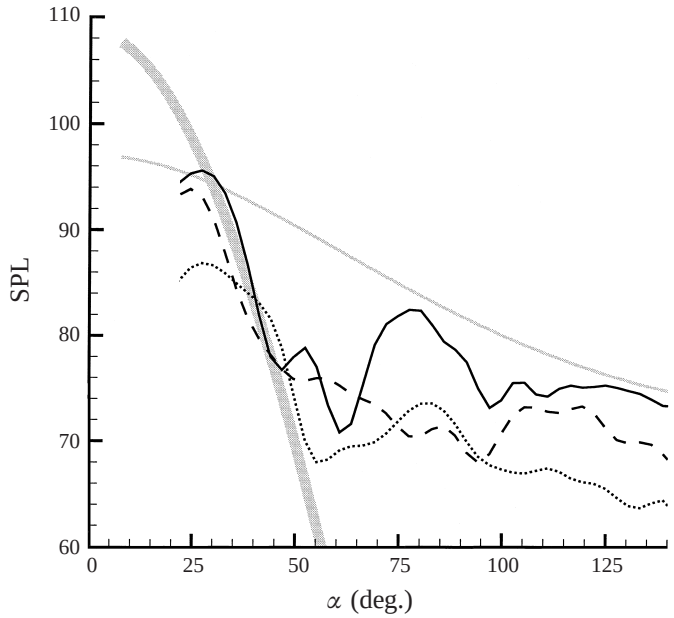

FIGURE 21. Sound pressure level directivity at $60r_o$ from the jet for individual source modes (see text): ———, $St_D = 0.19$; – – – –, $St_D = 0.29$; · · · · · ·, $St_D = 0.38$. Included for reference, the thick grey line is $\sim \exp[25 \cos\alpha]$, and the thin grey line is $\sim (1 - M_c \cos\alpha)^{-5}$.

sound pressure level directivity for this and two higher frequencies are shown in figure 21. None of these is well fitted in detail by (5.11), but the 20 dB drop between $\alpha \approx 30^\circ$ and $\alpha \approx 50^\circ$ would correspond roughly to $A = 25$ in (5.11). This curve is included on the plot for reference, as is the $(1 - M_c \cos\alpha)^{-5}$ estimate for convected quadrupoles (Ffowcs Williams 1963) with $M_c = 0.5$. Clearly the decay rate at small angles is faster than the convected quadrapole model would predict, but there is also an insufficient range of rapid decay to precisely determine its functional form. The form of the source suggests that it could indeed be exponential. The statistical sample is also insufficient to converge the directivity at larger angles from the jet, but the general trend here is closer to the slope of the $(1 - M_c \cos\alpha)^{-5}$ curve. Because of the rapid

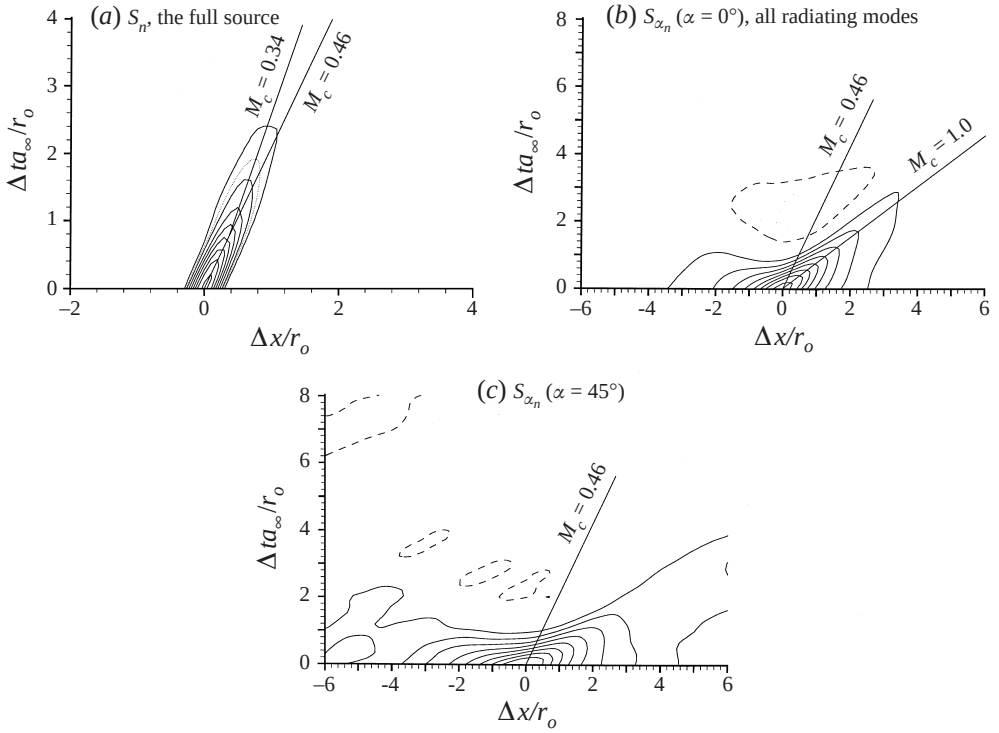

FIGURE 22. Space–time correlations at $r = r_o$ and $x = x_o = 20r_o$ that are defined by $\overline{S(x_o,t_o)S(x_o+\Delta x,t_o+\Delta t)}/\overline{S(x_o,t_o)S(x_o,t_o)}$ where S is: (*a*) the full acoustic source from (5.6); (*b*) the radiating source (to all angles) from (5.12); and (*c*) the source that radiates to angles $\alpha > 45°$ and $\alpha < 135°$. Contours show the 0.1 to 0.9 correlation isolevels (———) and the −0.1 isolevel (– – – –). The ····· contour in (*a*) is the 0.15 correlation isolevel. Straight lines show various convection velocities.

decay with angle, it is understandable that the sound from the low wavenumbers of the wave-packet envelope might be overwhelmed by other components at larger α.

5.6. *Source correlations and acoustic compactness*

At Mach 0.9 we do not expect the source to be acoustically compact, but understanding the degree to which it is non-compact is important for extension of low Mach number theory to near sonic conditions. Space–time and two-point correlations can provide a length scale for estimating source compactness (relative to the noise wavelength). Based upon figure 19, it is clear that at a single frequency the radiating source is on the scale of the whole jet. Although the distance over which individual modes remain correlated is evidently quite large (figure 19), the statistical correlation of the full source has also been used at times to estimate the source size. For example, an acoustically compact correlation length is an assumption made in developing the Lighthill/Ffowcs Williams convected quadrupole model. The compactness of the sources responsible for different portions of the directivity curve can be ascertained by extending the definition of (5.7) to filter the portion of the acoustic sources that is responsible for radiation above a certain angle α

$$\hat{S}_{\alpha_n}(k,r,\omega;\alpha) = \begin{cases} \hat{S}_n(k,r,\omega) & \text{if} \quad |ka_\infty/\omega| < \cos\alpha, \\ 0 & \text{otherwise.} \end{cases} \tag{5.12}$$

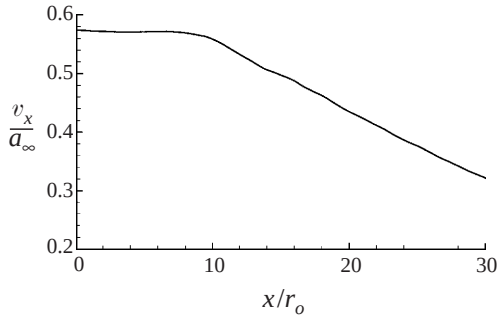

FIGURE 23. The mean Mach number at $r = r_o$ with respect to the ambient speed of sound.

The space–time correlation of $S(x, t)$, the full source from (5.6) including all frequencies and azimuthal modes, is shown in figure 22(*a*) and the space–time correlations of S_α, the inverse transform of $\hat{S}_{\alpha_n}$ in (5.12), with $\alpha = 0^\circ$ and 45° are shown in figures 22(*b*) and 22(*c*). Evidently the full source (figure 22*a*) is dominated by relatively small scales that convect with the flow. This is consistent with the visualization in figure 13. Only the correlations at $r = r_o$ and $x = 20r_o$ are shown, but these are typical for all positions in the turbulent flow (taking into account changes in the mean flow velocity as a function of position). The local convection Mach number of sources estimated from the slope of the straight line in the figure is $M_c = U_c/a_\infty = 0.46$ which roughly agrees with the value for the mean Mach number (figure 23) to within the accuracy of this estimation procedure. Close inspection of figure 22(*a*) also reveals a slight deceleration of the sources as they convect. Between $\Delta t a_\infty/r_o = 1$ and 2, the peak correlation at a given time no longer falls on the line corresponding to $M_c = 0.46$, but instead $M_c = 0.34$ appears to be a better fit with presumably a continuous deceleration between these estimates and beyond. The apparent deceleration is more rapid than the mean flow deceleration seen in figure 23. The reason for this discrepancy is unclear. However, it is not surprising that there is some decrease given the decrease of the mean.

In figure 22(*b*), it is apparent that the radiating (to all angles) component of the source is correlated over a much greater distance in the axial direction than was the full source, with $\ell_x \approx 4r_o$ giving the 20% correlation distance. Dominant frequencies for the acoustic radiation are primarily in the range $0.2 \lesssim St_D \lesssim 0.5$, so typical wavelengths are such that $5r_o < \lambda < 12r_o$. Thus, the source does not satisfy a $\lambda \gg \ell$ compactness condition. Higher frequency sources would be relatively less compact by the measure we have used, but the present data have insufficient statistical sample size to perform such an analysis reliably at individual frequencies. In figure 22(*b*) there is an apparent component of the source that convects with a near-sonic velocity, though this does not necessarily imply that turbulent eddies themselves convect at this speed.

Considering only components of the source that radiate at angles $\alpha > 45^\circ$ (figure 22*c*), we see that this portion of the source is even more correlated in the streamwise directions, with the 20% x-correlation distance now $\ell_x \approx 7r_o$. There is potentially a slight bias in the correlation along a line that would represent $M_c \approx \sqrt{2}$ ($\alpha = 45^\circ$), but this is minor, and for $\alpha > 45^\circ$ the radiating portion of the source appears to be nearly stationary. The time over which the source remains correlated does not increase as the source is filtered.

Both the full source and the two filtered sources considered above are compact in the radial direction as shown in figure 24. Again only correlations at $x = 20r_o$ and

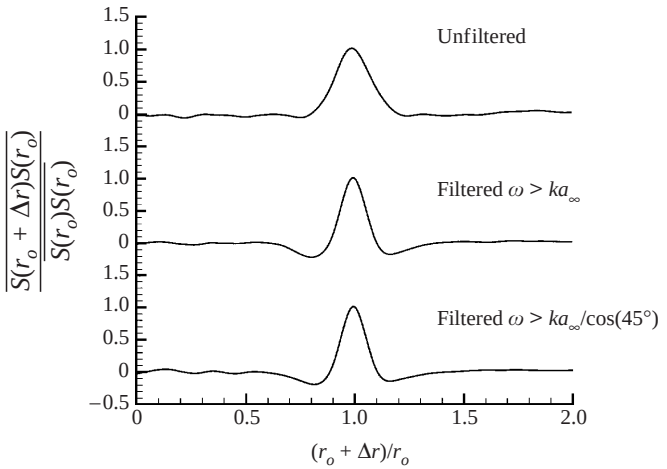

FIGURE 24. Radial correlation of the acoustic source at $x = 20r_o$, $r = r_o$.

$r = r_o$ are shown but these are typical of elsewhere in the jet. An implication of this is that each radial location in the jet radiates independently which in turn implies that the sound radiated from $r = 0$ would be refracted more than sound emitted near the edge of the jet flow. A single correction for refraction effects might therefore be an oversimplification.

6. Summary

This paper reports on a successful computation of subsonic turbulent jet noise from first principles. The results show excellent agreement with the experimental data of Stromberg *et al.* (1980) for both the mean flow development and the radiated sound. Computed Reynolds stresses are similar to those measured in similar jets, though the simulation jet is by necessity of low Reynolds number, which leads to several well-known differences from high Reynolds number jets. Despite this, visualizations show that the jet appears to be turbulent before the end of the potential core, which is supported by spectra, two-point velocity correlations, and the budget of turbulent kinetic energy.

For the first time the Lighthill source in a jet, which has been modelled by various methods in the past, was computed by Fourier methods to isolate the portion of the source that may radiate to the far field. To validate the implementation, it was shown that the sound could be accurately computed by solving Lighthill's equation. The source was then analysed in detail. It was first observed that the radiating portion of the source was largest in a different region of the jet than the peak intensity of the full source. Likewise, the mean turbulent kinetic energy and the mean radiating source were not well correlated. Filtering non-radiating modes from the source revealed that even in this turbulent flow the radiating portion of the source was roughly similar to that observed in laminar mixing layers (Colonius *et al.* 1997) or as might be predicted by linear stability analysis. The noise from these individual modes was analysed and found to be highly directional, much more so than typical Doppler factors would indicate. The acoustic compactness of the source was studied with space–time correlations that showed that its radiating component was not acoustically compact in the streamwise direction. The non-compactness was found to be more pronounced

for the portion of the source that radiated sound at larger angles from the jet axis. Space–time correlations also suggested that this portion of the source was stationary.

The author thanks Professor Tim Colonius for many helpful discussions and comments on this work, particularly with regard to filtering the acoustic sources, and Professor Thomas Bewley for his detailed comments on a draft of this paper. A portion of the simulation framework for this effort was developed by the author while a student of Professor Sanjiva Lele and Professor Parviz Moin at Stanford University. Financial support from NASA is gratefully acknowledged.

Appendix. Computing the sound beyond the flow computation

A short distance from the jet the flow is irrotational and has a negligible mean Mach number so low-amplitude (linear) pressure disturbances are accurately described by the homogeneous wave equation,

$$p_{tt} - a_\infty^2 \Delta p = 0. \tag{A 1}$$

Since the transformed pressure, $\hat{p}_n(k, r, \omega)$, is available from our source computations in § 5, it is straightforward to incorporate (A 1) into a boundary value formulation with $\hat{p}_n(k, r, \omega)$ given on a cylindrical shell at $r = R$, which is within the physical portion of the Navier–Stokes computation but beyond the jet flow itself. Applying (5.3) to (A 1) gives

$$\frac{\mathrm{d}^2 \hat{p}_n}{\mathrm{d}r^2} + \frac{1}{r}\frac{\mathrm{d}\hat{p}_n}{\mathrm{d}r} + \left[\omega^2 - k^2 - \frac{n^2}{r^2}\right]\hat{p}_n = 0. \tag{A 2}$$

A radiation condition at $r \to \infty$ restricts the solution to be

$$\hat{p}_n(k, r, \omega) = \begin{cases} \hat{p}_n(k, R, \omega) H_n^{(1)}(r\sqrt{\omega^2 - k^2}) / H_n^{(1)}(R\sqrt{\omega^2 - k^2}) & \text{if} \quad \omega > 0, \\ \hat{p}_n(k, R, \omega) H_n^{(2)}(r\sqrt{\omega^2 - k^2}) / H_n^{(2)}(R\sqrt{\omega^2 - k^2}) & \text{if} \quad \omega < 0, \end{cases} \tag{A 3}$$

where $H_n^{(1)}$ and $H_n^{(2)}$ are Hankel functions of the first and second kind respectively. Inverse transforming using (5.4) gives $p(x, r, \theta, t)$ in $r > R$. Only modes with $\omega > k$ radiate, so other modes are neglected in this study.

REFERENCES

Arndt, R. E. A., Long, D. F. & Glauser, M. N. 1997 The proper orthogonal decomposition of pressure fluctuations surrounding a turbulent jet. *J. Fluid Mech.* **340**, 1–33.

Bailly, C., Lafon, P. & Candel, S. 1994 Computation of subsonic and supersonic jet mixing noise using a modified k–ε model for compressible free shear flows. *Acta Acoustica* **2**, 101–112.

Bailly, C., Lafon, P. & Candel, S. 1997 Subsonic and supersonic jet noise predictions from statistical source models. *AIAA J.* **35**, 1688–1696.

Bastin, F., Lafon, P. & Candel, S. 1997 Computation of jet mixing noise due to coherent structures: the plan jet case. *J. Fluid Mech.* **335**, 261–304.

Boersma, B. & Lele, S. K. 1999 Large eddy simulation of a Mach 0.9 turbulent jet. *AIAA Paper* 99-1874.

Bogey, C., Bailly, C. & Juvé, D. 2000 Computation of the sound radiated by a 3-D jet using large eddy simulation. *AIAA Paper* 2000-2009.

Choi, D., Barber, T. J., Ciappetta, L. M. & Nishimua, M. 1999 Large eddy simulation of high-Reynolds number jet flows. *AIAA Paper* 99-0230.

Colonius, T., Lele, S. K. & Moin, P. 1993 Boundary conditions for direct computation of aerodynamic sound generation. *AIAA J.* **31**, 1174–1582.

Colonius, T., Lele, S. K. & Moin, P. 1997 Sound generation in a mixing layer. *J. Fluid Mech.* **330**, 375–409.

Crighton, D. G. 1975 Basic principles of aerodynamic noise generation. *Prog. Aerospace Sci.* **16**, 31–96.

Crighton, D. G. 1993 Computational aeroacoustics for low Mach number flows. In *Computational Aeroacoustics*, pp. 51–68. Springer.

Crighton, D. G. & Huerre, P. 1990 Shear-layer pressure fluctuations and superdirective acoustic sources. *J. Fluid Mech.* **220**, 255–368.

Crow, S. C. 1970 Aerodynamic sound emission as a singular perturbation problem. *Stud. Appl. Maths* **49**, 355–368.

Crow, S. C. 1972 Acoustic gain of a turbulent jet. *Bull. Am. Phys. Soc.* Paper IE. 6.

Doak, P. E. 1972 Analysis of internally generated sound in continuous materials: 2. A critical review of the conceptual adequacy and physical scope of existing theories of areodynamic noise, with special reference to supersonic jet noise. *J. Sound Vib.* **25**, 263–335.

Fedorchenko, A. T. 2000 On some fundamental flaws in present aeroacoustic theory. *J. Sound Vib.* **232**, 719–782.

Ffowcs Williams, J. E. 1963 The noise from turbulence convected at high speed. *Phil. Trans. R. Soc. Lond.* A **255**, 469–503.

Ffowcs Williams, J. E. & Kempton, A. J. 1978 The noise from the large-scale structure of a jet. *J. Fluid Mech.* **84**, 673–694.

Freund, J. B. 1999*a* Acoustic sources in a turbulent jet: a direct numerical simulation study. *AIAA Paper* 99-1858.

Freund, J. B. 1999*b* Direct numerical simulation of the noise from a Mach 0.9 jet. *ASME FEDSM* 99-7251.

Freund, J. B. 2000 A simple method for computing far-field sound in aeroacoustic computations. *J. Comput. Phys.* **157**, 796–800.

Freund, J. B., Lele, S. K. & Moin, P. 2000 Compressibility effects in a turbulent annular mixing layer. Part 1. Turbulence and growth rate. *J. Fluid Mech.* **421**, 229–267.

Freund, J. B. & Moin, P. 2000 Jet mixing enhancement by high amplitude fluidic actuation. *AIAA J.* **38**, 1863–1870.

Freund, J. B., Moin, P. & Lele, S. K. 1997 Compressibility effects in a turbulent annular mixing layer. *Tech. Rep.* TF-72, Stanford University, Mechanical Engineering, Flow Physics and Computation Division.

Goldstein, M. E. 1975 The low frequency sound from multipole sources in axisymmetric shear flows, with applications to jet noise. *J. Fluid Mech.* **70**, 595–604.

Goldstein, M. E. 1976 *Aeroacoustics.* McGraw-Hill.

Goldstein, M. E. 1982 High frequency sound emission from moving point multipole sources embedded in arbitrary transversely sheared mean flows. *J. Sound Vib.* **80**, 499–522.

Goldstein, M. E. 1991 Noise from turbulent shear flows. In *Aeroacoustics of Flight Vehicles* (ed. H. Hubbard). NASA RP 1258.

Huerre, P. & Crighton, D. G. 1983 Sound generation by instability waves in a low Mach number jet. *AIAA Paper* 83-0661.

Hussein, H. J., Capp, S. P. & George, W. K. 1994 Velocity measurements in a high-Reynolds-number, momentum-conserving, axisymmetric, turbulent jet. *J. Fluid Mech.* **258**, 31–75.

Khavaran, A. 1999 Role of anisotropy in turbulent mixing noise. *AIAA J.* **37**, 832–841.

Khavaran, A., Krejsa, E. A. & Kim, C. M. 1994 Computation of supersonic jet mixing noise for an axisymmetric convergent-divergent nozzle. *J. Aircraft* **31**, 603–609.

Laufer, J. & Yen, T.-C. 1983 Noise generation by a low-Mach-number jet. *J. Fluid Mech.* **134**, 1–31.

Lele, S. K. 1992 Compact finite difference schemes with spectral-like resolution. *J. Comput. Phys.* **103**, 16–42.

Lighthill, M. J. 1952 On sound generated aerodynamically: I. General theory. *Proc. R. Soc. Lond.* A **211**, 564–587.

Lighthill, M. J. 1954 On sound generated aerodynamically: II. Turbulence as a source of sound. *Proc. R. Soc. Lond.* A **222**, 1–32.

Lighthill, M. J. 1963 Jet noise. *AIAA J.* **1**, 1507–1517.

Lilley, G. M. 1974 On the noise from jets. *Tech. Rep.* CP-131. AGARD.

Lilley, G. M. 1991 Jet noise: Classical theory and experiments. In *Aeroacoustics of Flight Vehicles* (ed. H. Hubbard). NASA RP 1258.

Lush, P. A. 1971 Measurements of subsonic jet noise and comparison with theory. *J. Fluid Mech.* **46**, 477–500.

Mani, R. 1974 Further studies on moving source solutions relevant to jet noise. *J. Sound Vib.* **35**, 101–117.

Mollo-Christensen, E., Kolpin, M. A. & Martucelli, J. R. 1964 Experiments on jet flows and jet noise far-field spectra and directivity patterns. *J. Fluid Mech.* **18**, 285–301.

Panchapakesan, N. R. & Lumley, J. L. 1993 Turbulence measurements in axisymmetric jets of air and helium. Part 1. Air jets. *J. Fluid Mech.* **246**, 197–223.

Stromberg, J. L., McLaughlin, D. K. & Troutt, T. R. 1980 Flow field and acoustic properties of a Mach number 0.9 jet at a low Reynolds number. *J. Sound Vib.* **72**, 159–176.

Yen, C. & Messersmith, N. 1999 The use of compressible parabolized stability equations for prediction of jet instabilities and noise. *AIAA Paper* 99-1859.